Improving the cycling stability of Sn_4P_3 anode for sodium-ion battery

Wenhui Wang [a], Jiaolong Zhang [b], Denis Y.W. Yu [b], Quan Li [a, *]

[a] Department of Physics, The Chinese University of Hong Kong, Shatin, New Territory, Hong Kong
[b] School of Energy and Environment, City University of Hong Kong, Kowloon, Hong Kong

HIGHLIGHTS

- Sn agglomerates in Sn_4P_3 anode for Na-ion batteries upon cycling.
- Sn agglomeration identified as a major contributor to the anode capacity decay.
- Anode volume expansion does not significantly affect the anode cyclability.
- TiC additive effectively suppress Sn agglomeration and improve cyclability of Sn_4P_3.
- High volumetric capacity of the anode benefits from the high density TiC additive.

ARTICLE INFO

ABSTRACT

Experimental results from electrochemical characterizations and ex-situ X-ray diffraction (XRD) of the Sn_4P_3 anode upon cycling reveal that Sn agglomeration from the Sn_4P_3 particles plays a major role in the fast capacity fading of the Sn_4P_3 anode for sodium-ion batteries. TiC is demonstrated to be an effective additive to enhance the cycle stability of Sn_4P_3 by suppressing Sn agglomeration during cycling. Sn_4P_3/30-wt%TiC composite delivers a stable capacity of 300 mAh g^{-1} or 700 Ah L^{-1} over 100 cycles at current density of 100 mA g^{-1}. The high density TiC (4.93 g cm^{-3}), as compared to conventional carbon based additives, makes it attractive for achieving higher volumetric capacity of the anode.

1. Introduction

Sodium-ion battery (SIB) attracts great interest as an alternative for lithium-ion battery (LIB) mainly due to the abundance and uniform distribution of Na supplies. It has great potential in large scale energy storage applications. However, practical implementation of sodium technology is challenging due to the limited choice of anodes, an ideal choice of which should have high capacity, low average voltage, and good cycle stability [1,2].

Among various material choices [1,3–5], both Sn and P stand out due to their low average operating voltage (0.25 and 0.6V vs. Na/Na$^+$ for Sn and P, respectively) and large theoretical capacity (847 mAh g^{-1} and 2596 mAh g^{-1} for Sn and P, respectively, the highest two among all known anode materials) [1], making them promising SIB anode candidates with high energy density.

However, both Sn and P suffer from severe capacity decay during cycling [6,7]. Yang's group [8] proposed that the combination of Sn and P can lead to improved electrochemical performance, in particular, improving the cycle stability of the electrode, as Sn acts as electronic conductive channels to the less conductive but electrochemically active P, while P and/or its sodiated product (Na$_3$P) serve as host matrix to alleviate agglomeration of Sn and reduce the stress level in the electrode during charge/discharge process [8]. An average voltage of ~0.5V vs. Na/Na$^+$ and a theoretical capacity of 1132 mAh g^{-1} make Sn_4P_3 very attractive in SIB. Sn_4P_3, with an average voltage of ~0.9V vs. Li/Li$^+$ and a theoretical capacity of 1230 mAh g^{-1}, has also been investigated as a potential anode material for LIB [9–14]. Nonetheless, it is not a most popular system in LIB due to the presence of many promising anode candidates with better electrochemical performance such as Si, which has a theoretical capacity of 4200 mAh g^{-1} and average voltage of ~0.4V vs. Li/Li$^+$ [15]. The record performance of Sn_4P_3-based electrode in LIB was reported by Liu's group [13]—a capacity of 488 mAh g^{-1} was

* Corresponding author.
  E-mail address: liquan@phy.cuhk.edu.hk (Q. Li).

retained after 150 cycles at 100 mA g^{-1}.

While in SIB, Qian et al. [8] reported that Sn_4P_3/C (7:3, by weight) composites can deliver a reversible capacity of ~500 mAh (g^{-1} Sn_4P_3) after 150 cycles at 100 mA g^{-1}. Li et al. [16] showed Sn_4P_3-rGO (~9:1, by weight) with 3D mesoporous architecture delivers a reversible capacity of ~656 mAh (g^{-1} Sn_4P_3-rGO) over 100 cycles at 100 mA g^{-1}. Despite of the promising results obtained, one shall notice that most of the reported data employed carbon based materials as additives. If pure Sn_4P_3 is employed instead, capacity decays to <100 mA g^{-1} in the first 20 cycle [17]. The capacity fading of pure Sn_4P_3 was intuitively ascribed to the large volume expansion (~430%) of the anode material during the sodiation process in most of the works. Consequently, introducing large amount of carbon based materials (~30 wt% is commonly used for ball milled samples) and/or creating porous structure were expected to reduce the stress built-up during charge/discharge cycles [8,16,17]. Despite the improved capacity retention, the introduction of carbon material or porous structure significantly reduces the volumetric capacity of the electrode.

In the present work, we show that Sn agglomeration from pristine Sn_4P_3 particles, instead of volume expansion of the anode, mainly contributes to its capacity fading in the present experimental scheme. By introducing TiC into Sn_4P_3, Sn agglomeration is effectively suppressed and cycle stability is significantly improved. At the same time, the high density of TiC (4.93 g cm^{-3}) leads to small reduction in the volumetric capacity of the anode. Among all samples investigated, Sn_4P_3/TiC composite with 30 wt% TiC delivers a stable capacity of 300 mAh g^{-1} (normalized to the composite weight) or 700 Ah L^{-1} (estimated based on the density of sodiated phase) over 100 cycles at current density of 100 mA g^{-1}.

2. Experimental

2.1. Preparation of the Sn_4P_3/TiC composite

Sn_4P_3/TiC composite was prepared via a two-step high energy mechanical milling (HEMM) (Fritsch, Premium line Pulverisette 7) with tungsten carbide balls and container (80 mL).

In the first step, Sn_4P_3 powder was prepared by using Sn (Aldrich, <150 μm, 99.5%) and amorphous red phosphorus powders (Alfa Aesar, ~100mesh, 98.9%) in a molar ratio of 6:4. Note that, extra Sn (~9 wt%) was used in order to avoid possible P residues. HEMM was carried out under Ar atmosphere at 400 rpm for 30 h with balls to powder ratio of 10:1.

In the second step, the "pre-alloyed" Sn_4P_3 powder was milled with different amounts (0-30 wt%) of TiC (Alfa Aesar, 99.5%) to form Sn_4P_3/TiC composite. HEMM was carried out under Ar atmosphere at 400 rpm for 3 h with balls to powder ratio of 20:1. And the final composites were denoted as Sn_4P_3 (sometimes as Sn_4P_3/0TiC for comparison purpose), Sn_4P_3/10TiC, Sn_4P_3/20TiC, and Sn_4P_3/30TiC.

2.2. Characterizations

The crystallinity of the samples was examined by X-ray diffraction (XRD, SmartLab, Rigaku) with a Cu Kα radiation source (λ = 0.1541 nm). The XRD patterns of Sn_4P_3/TiC composite and the electrodes were collected with a scan rate of 8° min^{-1} under 40 kV and 40 mA, and a scan rate of 0.2° min^{-1} under 40 kV and 80 mA, respectively. In order to avoid any possible exposure to air, the electrodes were sealed with 2 mil Kapton tape in argon-filled glove box before XRD experiments. The morphologies of the samples were characterized by a field emission scanning electron microscope (FESEM, Quanta 200, FEI). Transmission electron microscopy (TEM FEI Tecnai F20ST) equipped with an energy dispersive spectrum X-ray detector (EDS) was carried out to study the detailed

microstructure and spatial distribution of the compositional elements in the respective samples.

2.3. Assembly of cells and electrochemical measurements

The electrodes were prepared by mixing Sn_4P_3/TiC composites (active material) with acetylene black and sodium carboxymethyl cellulose (NaCMC) binder with a mass ratio of 80:10:10 in water to form homogeneous slurry. The slurry was then coated on Cu foil followed by vacuum drying at 60 °C overnight. Electrodes with diameter of 16 mm and active material loading of ~1.5 mg cm^{-2} were then cut out from the dried coating. Sn (Aldrich, 10 μm, 99%) electrode is also prepared in the same way as a control.

The electrodes were assembled into CR2032 coin-type cells with Na foil and glass fiber filter (GD-120) as reference electrode and separator, respectively. 1 M NaClO$_4$ in a mixture of propylene carbonate and fluoroethylene carbonate (PC/FEC, 95:5, by volume) was used as the electrolyte unless otherwise noted.

The Na-ion cells were galvanostatically charged/discharged using multichannel battery test system (Neware, Shenzhen). 10 min of rest was employed between each charge and discharge process. Cyclic voltammetry was carried out via electrochemical workstation (CHI 660C, Shanghai Chenhua Instrument Co., Ltd.). Thickness change of the electrode during charge and discharge was monitored using an electrochemical dilatometer (ECD-1, from EL-Cell) with Na metal foil as counter and reference electrode, and 1 M NaPF$_6$ in mixture of ethylene carbonate/diethyl carbonate (EC/DEC, 1:1 by vol) with additional 5 vol% FEC as the electrolyte. The detailed explanation on the electrode thickness test can be found in previous report [18]. All experiments were carried out at room temperature (24 ± 2 °C) unless specified otherwise.

3. Results and discussions

3.1. Capacity fading of pure Sn_4P_3

Fig. 1a shows the XRD pattern of the as-synthesized Sn_4P_3. All of the diffraction peaks can be indexed to the hexagonal Sn_4P_3 with space group of R-3m (PDF#73−1820). The lattice parameters obtained from the Rietveld refinement (agreement factor R_{wp} = 6.87%) are $a = b$ = 3.9915 Å and c = 35.4189 Å, which are amongst the values of the previous reports of Sn_4P_3 [19−21]. However, the EDX taken from the same sample show Sn/P has an atomic ratio of 6/4 with a uniform distribution (see Figs. S1 and S2), indicating there is extra Sn uniformly distributes in the sample. Since no diffraction peak of Sn can be found in the XRD, it should be due to either its low content, its highly nanocrystalline/amorphous nature, or additional Sn in the Sn_4P_3 lattice. SEM image in the inset of Fig. 1a shows that the size of these particles is in the range of a few hundred nanometers to a few microns.

Cyclic voltammogram of Sn_4P_3 electrode (Fig. S3) confirms the electrochemical activity of both Sn and P, which is consistent with previous report [21]. The cycle performance of the Sn_4P_3 electrode measured at a current density of 100 mA g^{-1} is shown in Fig. 1b. The first sodiation/de-sodiation capacities are 622.5 and 532.3 mAh g^{-1}, respectively, corresponding to a high initial coulombic efficiency (ICE) of 85.5%. This ICE is among the best in SIBs anodes [3,4,22]. It is worth noting that a higher ICE of the anode means fewer amount of Na-containing cathode is needed to match the initial irreversible Na loss in the anode, leading to a higher energy density in practical batteries [23−25]. The Sn_4P_3 electrode delivers a stable capacity of ~525 mAh g^{-1} for the first 40 cycles. However, it suffers from a fast decay afterwards, retaining only 17.4% of the initial de-sodiation capacity at the end of 100th cycles.

The change in electrochemistry along with the capacity fading of
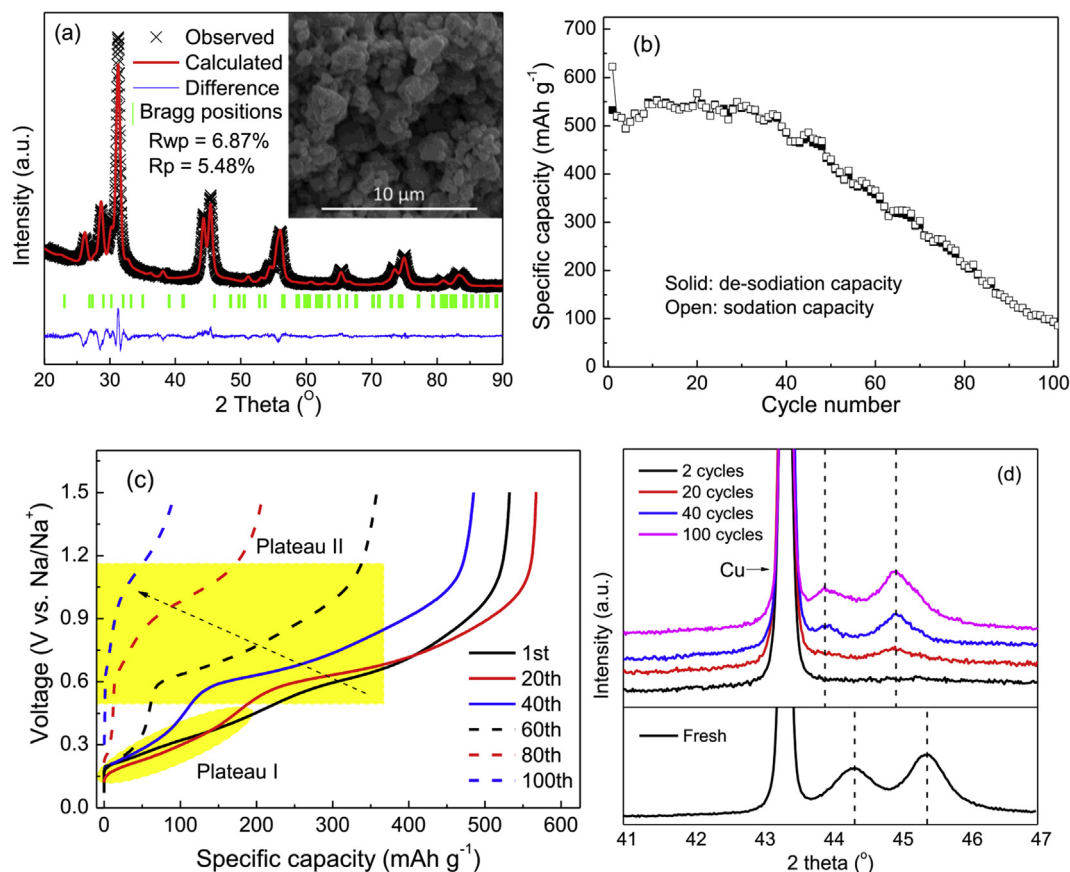
Fig. 1. (a) XRD pattern of ball milled Sn_4P_3, and insert shows the corresponding SEM image; (b) cycle performance and (c) evolution of de-sodiation voltage profiles of Sn_4P_3 in the voltage range of 1.5−0.01 V at 100 mA g^{-1}; (d) the ex-situ XRD patterns of Sn_4P_3 electrode after cycling in the voltage range of 1.5−0.01 V for specific cycles, and the dash lines in upper and lower frames indicate position of the diffraction peaks of Sn and Sn_4P_3, respectively.

the anode can be disclosed by the evolution of de-sodiation profiles with cycling. As shown in Fig. 1c, the 1st de-sodiation voltage profile is generally smooth, which is typical for active materials with small grain size and/or low crystallinity [9,26]. Two sloping voltage plateaus at about 0.3 and 0.6V (marked as plateau I and II in Fig. 1c, respectively) appear after 20 cycles. This is in fact similar to the de-sodiation voltage profile of pure Sn (SI, Fig. S4), which mainly originates from the de-sodiation of $Na_9Sn_4 \rightarrow NaSn \rightarrow NaSn_5$ [27]. Upon extended charge/discharge cycles, the capacity of plateau I gradually decreases and finally vanishes. The capacity of plateau II shows similar trends as plateau I, although it does not completely disappear up to 100th cycle. In addition, plateau II gradually shifts up to higher voltage upon repeated cycles, suggesting increased polarization in the sample. All of these changes in the de-sodiation profiles of the Sn_4P_3 suggest agglomeration of Sn from the original Sn_4P_3. In other word, after Sn_4P_3 is sodiated to Na_xSn_y ($Na_{15}Sn_4$ for complete sodiation) and Na_3P, the re-formation of Sn_4P_3 phase in the following de-sodiation process is difficult. With the continuous segregation of Sn phase, the Sn_4P_3 would become a physical mixture of separated Sn-rich or P-rich particles (Fig. S5) and the de-sodiation voltage profile deteriorate dramatically because of the sluggish Na^+ diffusion in Sn and poor electronic conductivity of P.

Ex-situ XRD data of the electrodes after different cycles were collected at the end of de-sodiation process (*i.e.* 1.5V). After two cycles, little diffraction signal of Sn- or P- based elements or compounds was detected (Fig. 1d), suggesting the final de-sodiation products are small grains and in highly dispersed states [9,11].

After 20 cycles, the diffraction peaks of Sn appear, revealing the aggregation of Sn clusters into crystalline Sn. At the same time, peaks corresponding to the crystalline phase of Sn_4P_3 are no longer detectable. Upon extended charge/discharge cycles, more crystalline Sn is witnessed by the increased intensity of the Sn diffraction peaks. Meanwhile, for the first 40 cycles, the aggregation of crystalline Sn is also evidenced by the obviously decreased full width at half maximum (FWHM) of Sn diffraction peak at ~44.95°. The agglomeration of Sn and P is also suggested by the existence of particles composed of mainly Sn or P in "Sn_4P_3" electrode after 100 cycles (Figs. S3 and S4).

In the literature, large volume changes during charge/discharge process is generally considered as an important factor causing capacity fading of Sn-based electrode [8,17]. To identify the correlation between capacity and the volume change of the electrode, we carried out in-situ dilatometry test to monitor the thickness change of Sn_4P_3 electrode along sodiation/de-sodiation process. Based on the in-situ thickness result (Fig. S6), the first sodiation capacity of 625 mAh g^{-1} in Fig. 1 b results in a ~110% increase in the thickness of the electrode. Nevertheless, such a large volume change does not lead to capacity fading of the electrode in the following cycle.

On the other hand, it has been suggested that potential confinement (charge/discharge test with confined upper voltage at 1.0V) can suppress Sn agglomeration, as documented in other Sn-based anodes [26,28,29], while retain a similar de-sodiation capacity and electrode volume change [5,30]. This is possible as the average potential of both Sn and P are well below 1.0V [1]. Fig. 2a and b compares the electrochemical performance of the electrodes
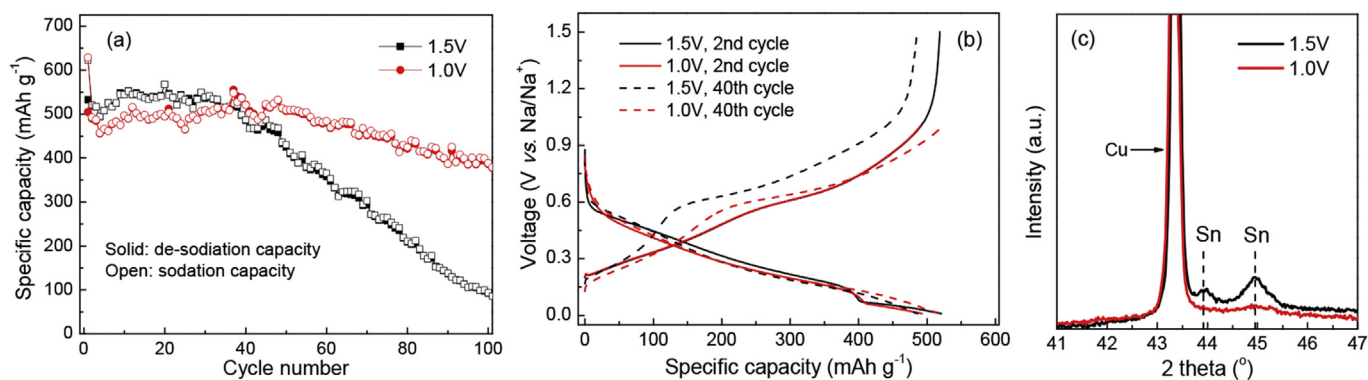
Fig. 2. (a) Cycle performance of Sn_4P_3 in the voltage range of 1.5–0.01 V and 1.0–0.01 V; (b) comparison of 2nd and 40th charge/discharge curves in the voltage range of 1.5–0.01 V and 1.0–0.01 V, and (c) the corresponding ex-situ XRD patterns after 40 cycles.

when the upper voltage is set at 1.5V (unconfined) and 1.0V (confined) during cycling. As expected, the evolution of both voltage profiles (Fig. 2b) and ex-situ XRD patterns (Fig. 2c) reveal the suppression of Sn agglomeration via the potential confinement. The capacity retention over 100 cycles is significantly increased from 17.4% to 76.4% (Fig. 2a) despite of the similar electrode capacity before significant decay takes place at the end of ~40 cycles for samples processed at 1.5V. Note that one shall expect similar volume expansion when similar capacity is delivered (in the present case, the alloying mechanism determines the correlation between the capacity increase and volume expansion of the electrode [5,24,30]). Consequently, the potential confinement results suggest that the volume change of the anode should not significantly contribute to the fast capacity decay of the electrode.

3.2. Improving cycle stability of Sn_4P_3 anode by incorporating TiC

Fig. 3a shows the XRD patterns of Sn_4P_3/TiC composite with different TiC amounts (from 0 to 30 wt%). Additional diffraction peaks of TiC are observed after the incorporation of TiC, and the peak intensity relative to that of Sn_4P_3 increases with increasing TiC amounts. TiC shows negligible effect on the crystallinity of Sn_4P_3. SEM images (Fig. 3b and Fig. S7) reveal that TiC may lead to slight

aggregation of Sn_4P_3.

Fig. 4 shows the cycle performance of Sn_4P_3/TiC composites at a current density of 100 mA g^{-1}. Although the initial de-sodiation capacities of Sn_4P_3/TiC composites are lower than that of the pure Sn_4P_3 due to the presence of the inactive TiC phase (Fig. S8), their capacity retention over 100 cycles is significantly enhanced with increasing TiC amount: 17.4%, 41.1%, 82.9%, and 94.5% for 0, 10, 20, and 30 wt%. By estimating the density of Sn_4P_3 at the first sodiated state (see SI), the Sn_4P_3/20TiC composite delivers a similar volumetric capacity (~850Ah L^{-1}) to that of pure Sn_4P_3 (~900Ah L^{-1}). Even with 30 wt% TiC incorporation, the composite still delivers a reversible volumetric capacity of ~730Ah L^{-1}, which is much higher than the volumetric capacity of hard carbon (*i.e.* 450Ah/L [25]).

To understand the enhanced electrochemical performance of Sn_4P_3/TiC composites, the evolution of sodiation/de-sodiation voltage profiles of Sn_4P_3/TiC composites are compared. As shown in Fig. 5, when incorporated with 10 wt% and 20 wt% TiC, the appearance of voltage plateaus at 0.3 and 0.6 V are delayed, which indicates that the agglomeration of Sn is mitigated. Further increase of TiC amount to 30 wt% would larger defer the appearance of voltage plateaus at 0.3 and 0.6 V. The trend is consistent with the gradually increased capacity retention of Sn_4P_3/TiC composites with the increase of the TiC amount. These phenomena indicate
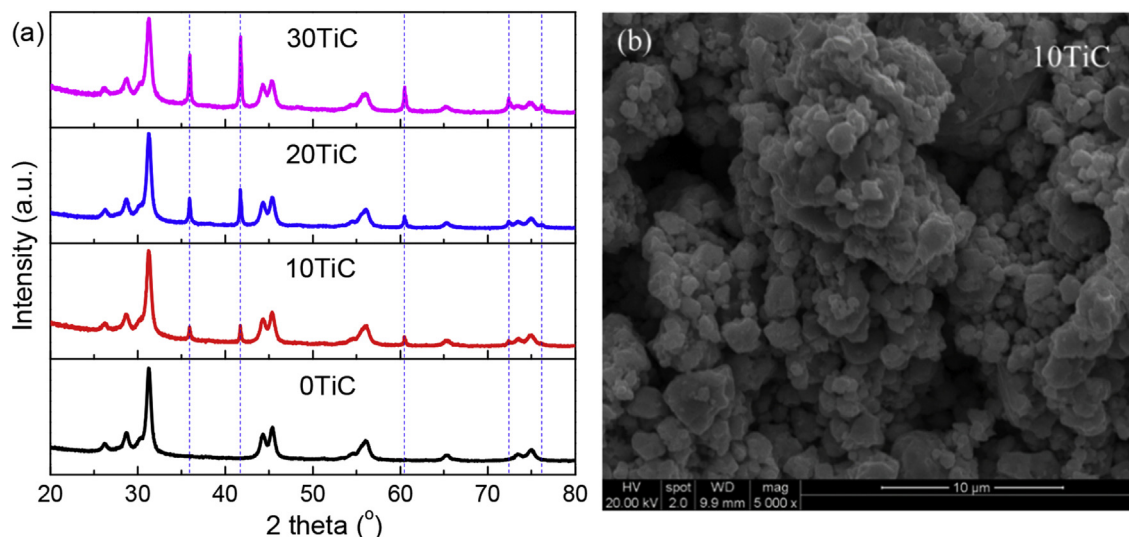
Fig. 3. (a) XRD patterns of Sn_4P_3/TiC composites with different TiC amounts, and the dash lines indicate position of the diffraction peaks of TiC; (b) SEM image of Sn_4P_3/10TiC composites, being representative of all samples tested.
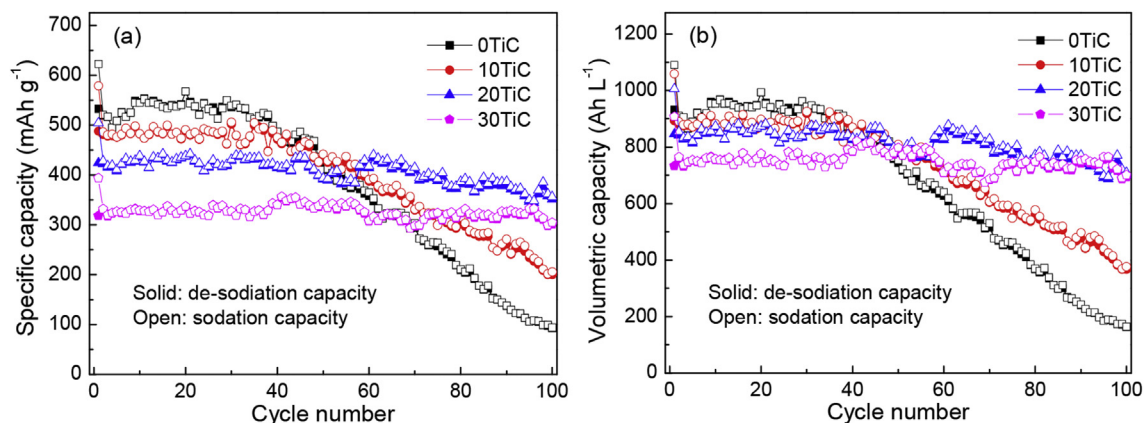
Fig. 4. (a) Cycle performance of Sn_4P_3/TiC composites in the voltage range of 1.5–0.01 V; and (b) the corresponding volumetric capacity calculated based on the density of the sodiated Sn_4P_3 and TiC phases.
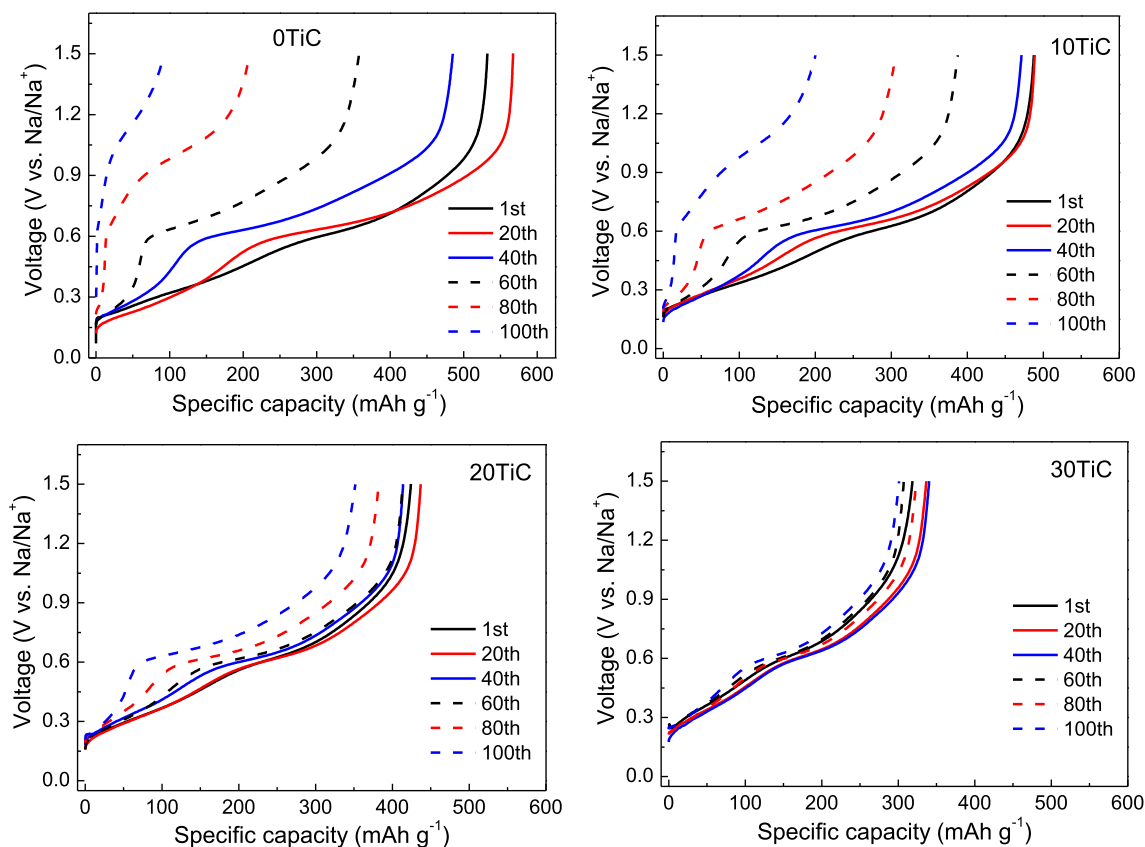
Fig. 5. Evolution of sodiation/de-sodiation voltage profile of Sn_4P_3/TiC composites electrode.

that the suppressed Sn agglomeration from Sn_4P_3 in the presence of TiC leads to the enhanced cycle stability of Sn_4P_3/TiC composites.

Ex situ XRD patterns of Sn_4P_3/20TiC composite electrode after different cycles were also collected. As can be seen from Fig. 6, the agglomeration of Sn from Sn_4P_3/20TiC composite electrode is significantly suppressed when compared to that in pure Sn_4P_3 electrode. A weak diffraction shoulder peak at ~45.48° suggests the reforming of Sn_4P_3 during cycling.

4. Conclusion

Sn agglomeration from Sn_4P_3 upon repeated cycles is suggested

as a major cause for the capacity fading of the electrode. Introducing TiC to Sn_4P_3 can suppress the Sn agglomeration to certain extend, and thus lead to enhanced cycling performance. In a batch of Sn_4P_3/TiC samples with different amount of TiC ranging from 0 wt% to 30 wt%, it was found that higher amount of TiC leads to more stable cycling performance. Among the samples, Sn_4P_3/30TiC retains 94.5% of its initial de-sodiation capacity at 100th cycle. The experimental results suggest a possible strategy to suppress Sn agglomerations during the cycling of Sn_4P_3, leading to improved cycle performance of the anode.
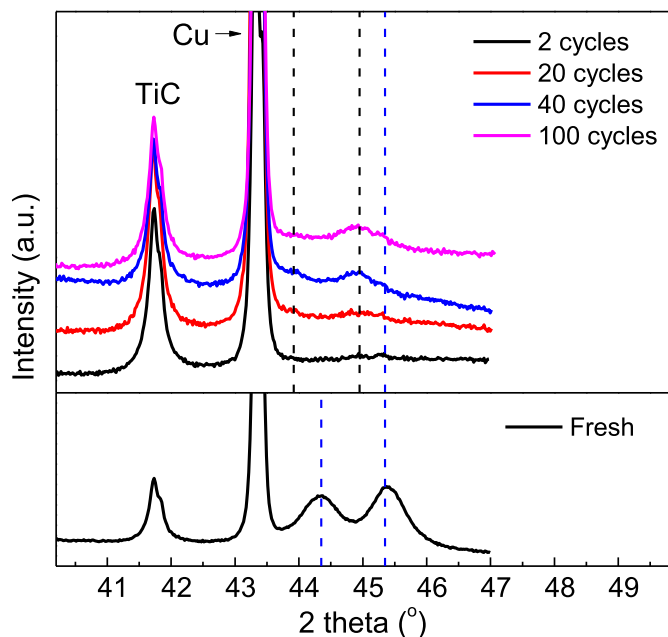
Fig. 6. Evolution of XRD patterns of Sn_4P_3/20TiC composite electrode after different cycles. The black dash lines indicate position of the diffraction peaks of Sn, while the blue dash lines indicate position of the diffraction peaks of Sn_4P_3. (For interpretation of the references to colour in this figure legend, the reader is referred to the web version of this article.)

Appendix A. Supplementary data

Supplementary data related to this article can be found at http://dx.doi.org/10.1016/j.jpowsour.2017.08.060.

References

[1] N. Yabuuchi, K. Kubota, M. Dahbi, S. Komaba, Chem. Rev. 114 (2014) 11636–11682.
[2] K. Kubota, S. Komaba, J. Electrochem. Soc. 162 (2015) A2538–A2550.
[3] D. Stevens, J. Dahn, J. Electrochem. Soc. 147 (2000) 1271–1273.
[4] S. Komaba, W. Murata, T. Ishikawa, N. Yabuuchi, T. Ozeki, T. Nakayama, A. Ogata, K. Gotoh, K. Fujiwara, Adv. Funct. Mater. 21 (2011) 3859–3867.
[5] V.L. Chevrier, G. Ceder, J. Electrochem. Soc. 158 (2011) A1011.
[6] S. Komaba, Y. Matsuura, T. Ishikawa, N. Yabuuchi, W. Murata, S. Kuze, Electrochem. Commun. 21 (2012) 65–68.
[7] W.J. Li, S.L. Chou, J.Z. Wang, H.K. Liu, S.X. Dou, Nano Lett. 13 (2013) 5480–5484.
[8] J. Qian, Y. Xiong, Y. Cao, X. Ai, H. Yang, Nano Lett. 14 (2014) 1865–1869.
[9] Y.-U. Kim, C.K. Lee, H.-J. Sohn, T. Kang, J. Electrochem. Soc. 151 (2004) A933.
[10] Y.-U. Kim, S.-I. Lee, C.K. Lee, H.-J. Sohn, J. power sources 141 (2005) 163–166.
[11] B. Leon, J.I. Corredor, J.L. Tirado, C. Perez-Vicente, J. Electrochem. Soc. 153 (2006) A1829.
[12] J.-J. Wu, Z.-W. Fu, J. Electrochem. Soc. 156 (2009) A22.
[13] S. Liu, H. Zhang, L. Xu, L. Ma, X. Hou, Electrochimica Acta 210 (2016) 888–896.
[14] S. Liu, H. Zhang, L. Xu, L. Ma, X. Chen, J. Power Sources 304 (2016) 346–353.
[15] A. Eftekhari, Energy Storage Mater. 7 (2017) 157–180.
[16] Q. Li, Z. Li, Z. Zhang, C. Li, J. Ma, C. Wang, X. Ge, S. Dong, L. Yin, Adv. Energy Mater. (2016) 1600376.
[17] J. Liu, P. Kopold, C. Wu, P.A. van Aken, J. Maier, Y. Yu, Energy Environ. Sci. 8 (2015) 3531–3538.
[18] D.Y.W. Yu, M. Zhao, H.E. Hoster, ChemElectroChem 2 (2015) 1090–1095.
[19] Y. Kim, Y. Kim, A. Choi, S. Woo, D. Mok, N.S. Choi, Y.S. Jung, J.H. Ryu, S.M. Oh, K.T. Lee, Adv. Mater. 26 (2014) 4139–4144.
[20] W. Li, S.L. Chou, J.Z. Wang, J.H. Kim, H.K. Liu, S.X. Dou, Adv. Mater. 26 (2014) 4037–4042.
[21] L. Zheng, R.A. Dunlap, M.N. Obrovac, J. Electrochem. Soc. 163 (2016) A1188–A1191.
[22] Y. Li, Y.-S. Hu, M.-M. Titirici, L. Chen, X. Huang, Adv. Energy Mater. (2016) 1600659.
[23] J.C. Burns, L.J. Krause, D.-B. Le, L.D. Jensen, A.J. Smith, D. Xiong, J.R. Dahn, J. Electrochem. Soc. 158 (2011) A1417.
[24] M. Obrovac, V. Chevrier, Chem. Rev. 114 (2014) 11444–11502.
[25] E. Irisarri, A. Ponrouch, M.R. Palacin, J. Electrochem. Soc. 162 (2015) A2476–A2482.
[26] I.A. Courtney, W. McKinnon, J. Dahn, J. Electrochem. Soc. 146 (1999) 59–68.
[27] L.D. Ellis, T.D. Hatchard, M.N. Obrovac, J. Electrochem. Soc. 159 (2012) A1801–A1805.
[28] O. Mao, J. Dahn, J. Electrochem. Soc. 146 (1999) 414–422.
[29] J. Fan, T. Wang, C. Yu, B. Tu, Z. Jiang, D. Zhao, Adv. Mater. 16 (2004) 1432–1436.
[30] M.N. Obrovac, L. Christensen, D.B. Le, J.R. Dahn, J. Electrochem. Soc. 154 (2007) A849.